Insight into the Microstructure and Ionic Conductivity of Cold Sintered NASICON Solid Electrolyte for Solid-State Batteries

Yulong Liu,[†] Jingru Liu,[‡] Qian Sun,[†] Dawei Wang,[†] Keegan R. Adair,[†] Jianneng Liang,[†] Cheng Zhang,[‡] Li Zhang,[∥] Shigang Lu,[∥] Huan Huang,[§] Xiping Song,*,[‡] and Xueliang Sun*,[†]

[†]Department of Mechanical and Materials Engineering, The University of Western Ontario, London, Ontario N6A 5B9, Canada

[‡]State Key Laboratory for Advance Metal and Materials, University of Science and Technology Beijing, Beijing 100083, China

[∥]China Automotive Battery Research Institute Co., Ltd, Beijing 100088, China

[§]Glabat Solid-State Battery Inc., 700 Collip Circle, Suite 211, London, Ontario N6G 4X8, Canada

S *Supporting Information*

ABSTRACT: $Li_{1.3}Al_{0.3}Ti_{1.7}(PO_4)_3$ (LATP) is a popular solid electrolyte used in solid-state lithium batteries due to its high ionic conductivity. Traditionally, the densification of LATP is achieved by a high-temperature sintering process (about 1000 °C). Herein, we report the compaction of LATP by a newly developed cold sintering process and post-annealing. LATP pellets are first densified at 120 °C and then annealed at 650 °C, yielding an ionic conductivity of 8.04×10^{-5} S cm^{-1} at room temperature and a relative density of 93% with a low activation energy of 0.37 eV. High-resolution transmission electron microscopy of the cold sintered pellets is investigated as well, showing that the particles are interconnected with some nanoprecipitates at the grain boundaries. Such nanocrystalline-enriched grain boundaries are beneficial for lithium-ion transportation, which leads to higher ionic conductivity of the cold sintered sample. This new sintering process can direct new horizons for development of all solid-state batteries due to its simplicity.

KEYWORDS: LATP, cold sintering process, ionic conductivity, HRTEM, solid-state electrolyte
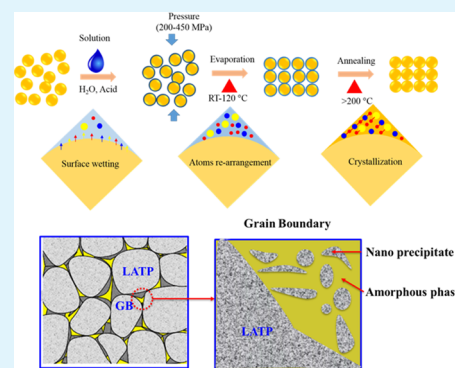
INTRODUCTION

Lithium-ion batteries have become one of the most indispensable energy storage devices, especially for their application in portable electronics.[1] Typically, traditional LIBs use liquid electrolytes, which are composed of Li salt and organic solvents. Unfortunately, liquid electrolyte-based batteries possess the risks of thermal runaway and even fire due to the flammability of the organic solvents.[1] Because of these hazards, the development of solid-state electrolytes was stimulated in the search for nonflammable batteries that are tolerant to extreme conditions. In the past years, numerous solid electrolytes have been synthesized based on oxide, sulfide, and solid polymer electrolyte chemistries.[2−5]

However, the overall ionic conductivity of most solid electrolytes is very low because of the limited lithium diffusivity at the grain boundaries. To improve the lithium conductivity, high-temperature sintering/annealing is usually needed to increase the transportation between grains, especially for oxides and sulfides.[6] Nevertheless, high temperatures may cause the evaporation of lithium from the compound, leading to the off-stoichiometry compositions of the solid electrolyte. The ionic conductivity of solid electrolytes is reduced after the change in composition.[7]

The annealing temperature for the oxide electrolytes is as high as 1000 °C during the densification process. In order to

decrease the densification time and temperature, pressure-assisted sintering techniques such as spark plasma sintering have been employed to facilitate the mass-transport process.[7,8] Alternatively, the cold sintering process (CSP) was recently developed by Randall's group and offers a route to the densification of ceramics at temperatures below 300 °C.[9−12] Such a low temperature is very attractive for the densification of solid electrolytes in counteracting the issues associated with the loss of lithium. Generally, the CSP involves a multistage nonequilibrium process such as dissolution−precipitation under external stress, viscous flow of saturated solutions, and diffusion of species.[13−16] There are already some initial mechanism studies in understanding the CSP, but there is still ambiguity in the exact underlying process that occurs.[17−19] Recently, Randall et al. has reported the synthesis of $Li_{1.5}Al_{0.5}Ge_{0.5}(PO_4)_3$ solid electrolyte with CSP, and it was shown to have an ionic conductivity of 5×10^{-5} S cm^{-1} at room temperature after annealing. This work exemplifies that CSP can be applied to the synthesis of solid electrolytes through lower temperature densification processes, which can avoid the evaporation of lithium.[19] In addition, there is a lack
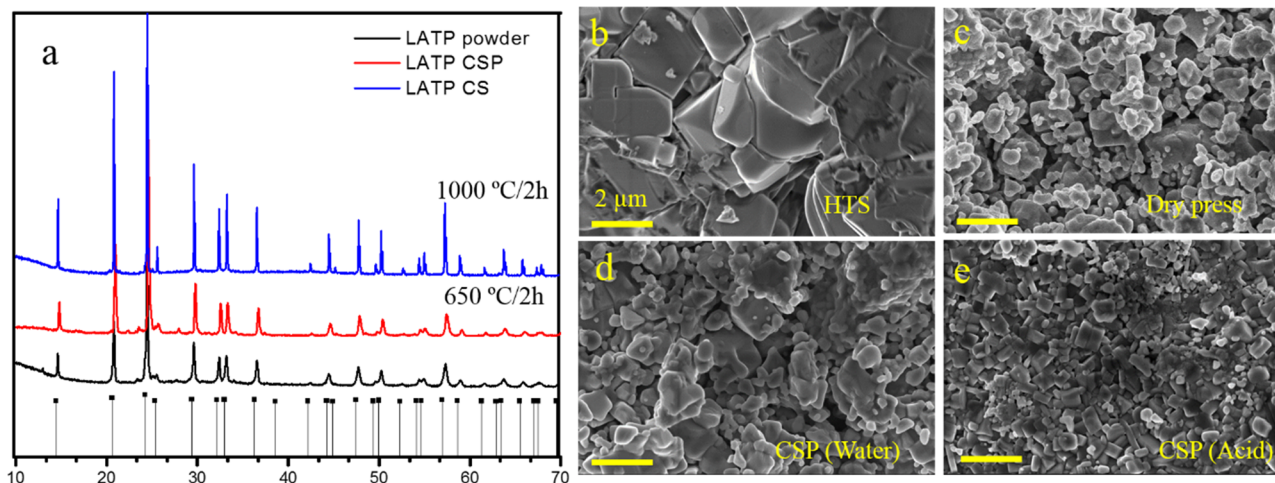
Figure 1. (a) XRD patterns of LATP electrolyte synthesized via high-temperature sintering and cold sintering process with acetic acid. SEM images of electrolytes fabricated by (b) high-temperature sintering (HTS), (c) dry-press sintering, (d) cold sintering with water, and (e) cold sintering with 1 M acetic acid.
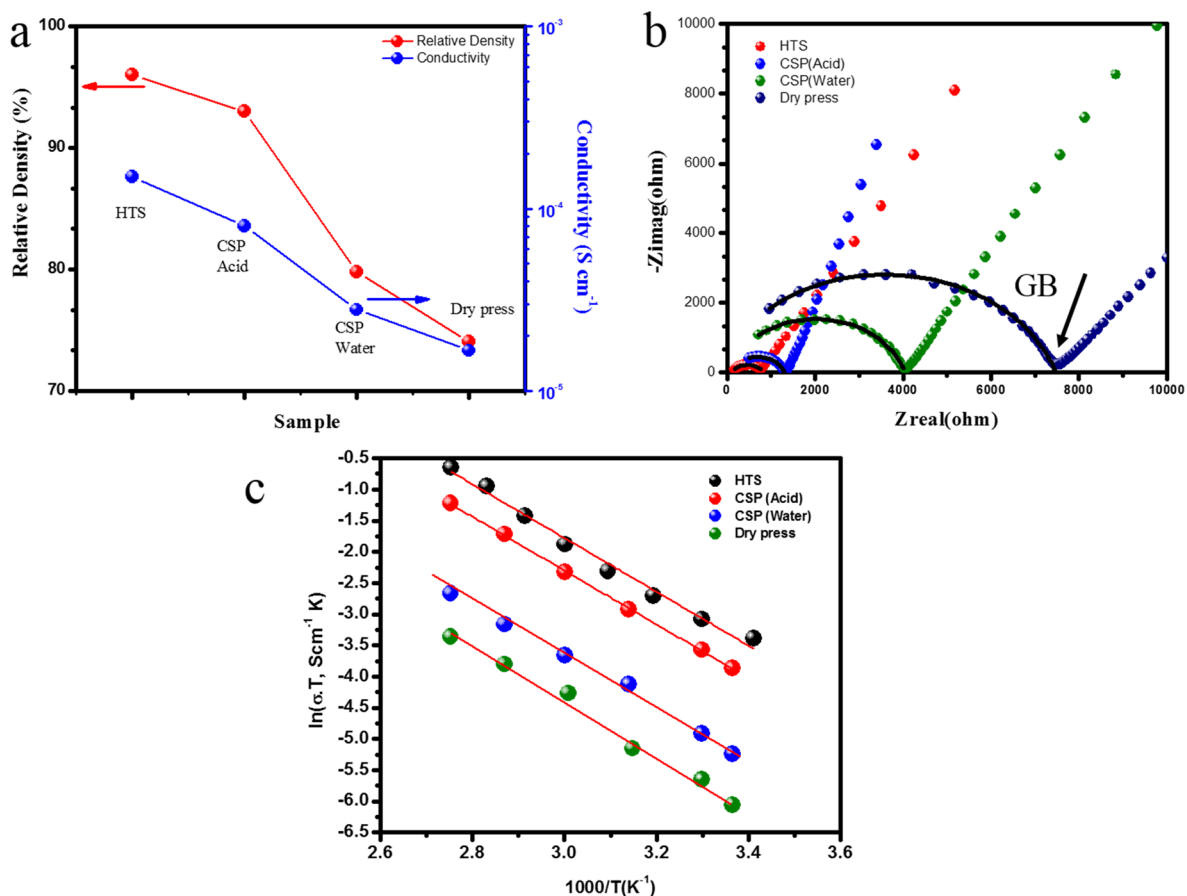

Figure 2. Effects of cold sintering on LATP electrolyte. (a) Density and ionic conductivity of LATP pellets at different sintering condition, (b) electrochemical impedance at room temperature, and (c) Arrhenius plots.

of investigation on the grain boundary structure of cold sintering solid electrolytes. It is known that the ionic conduction at the grain boundary plays a critical role in solid electrolytes. Thus, a detailed study on the microstructure is necessary in understanding its relationship with lithium-ion conductivity.

Li$_{1.3}$Al$_{0.3}$Ti$_{1.7}$(PO$_4$)$_3$ (LATP) electrolyte, a lithium conductor with NASICON structure, is prepared by CSP and post-annealing.[20] Herein, the mechanism of CSP-LATP electrolyte formation is explored and the effects of tuning the sintering conditions, solution effect, and applied stress are discussed. Through a systematic investigation of the CSP parameters, an LATP electrolyte with an ionic conductivity of 8.04×10^{-5} S cm^{-1} is obtained, with a relative density of 93% and activation energy of 0.37 eV. The microstructure analysis under TEM shows that the nanoparticles are precipitated at
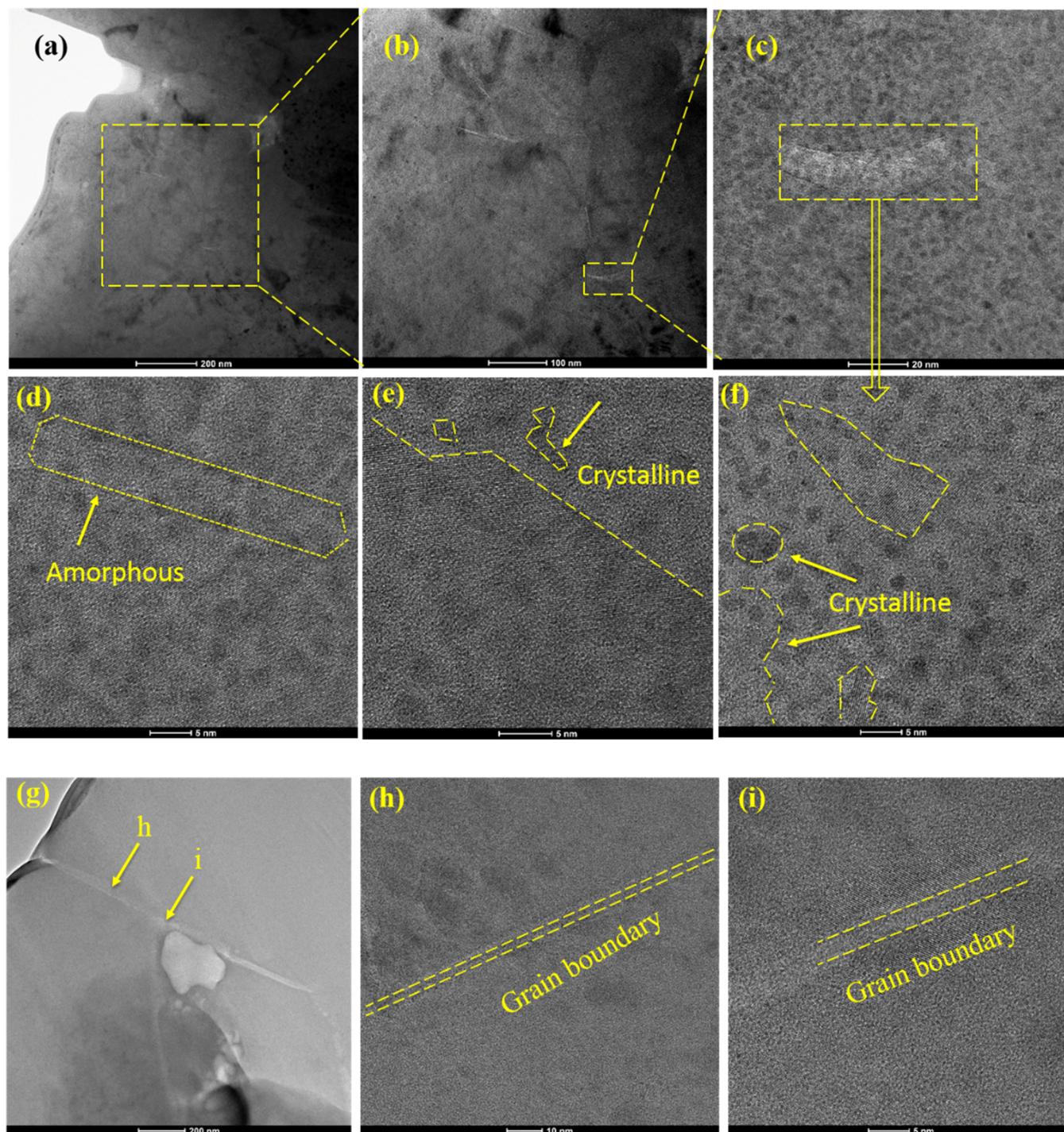
Figure 3. HRTEM images of CSP-LATP with (a−f) acetic acid and (g−i) HTS-LATP.

the grain boundary of the CSP-LATP, with a uniform chemical distribution across the particles.

RESULTS AND DISCUSSION

Figure 1a displays the XRD patterns of LATP under conventional high-temperature sintering (HTS, 1000 °C/2 h) and cold sintering processes (CSP, 120 °C/1 h + 650 °C/2 h). The obtained pellets exhibit similar diffraction pattern as the pristine LATP powders, with no extra peaks being detected. The XRD results indicate that the CSP did not introduce detectable impurities into the solid electrolyte.

The microstructure of the LATP electrolyte under different sintering processes is shown in Figure 1b−e. The cross-sectional images are obtained without additional polishing or thermal etching. For HTS-LATP, the powders are compacted under high temperature by forming a sintering neck between particles. The pristine powders are grown to micro-size due to the high temperature. If the LATP powders are pressed without any solution, a dry-press pellet is obtained and the cross section is demonstrated in Figure 1c. The dry-press pellet is porous, with loosely stacked powders. When adding water during the CSP process, the pellet becomes more densely packed compared to the dry-press LATP. Moreover, the
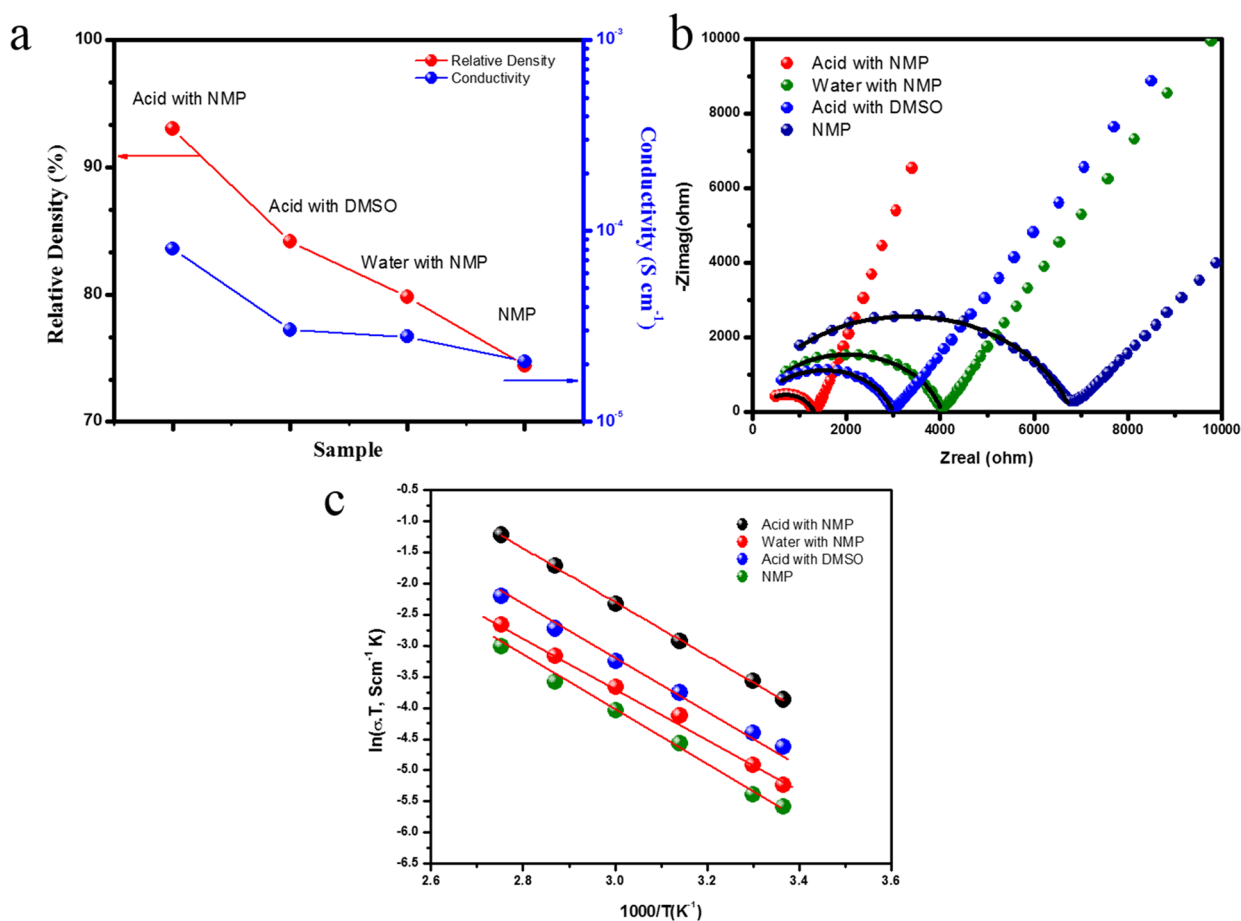
Figure 4. Solution effect of cold sintered LATP. (a) Density and ionic conductivity of cold sintered LATP pellets with different solutions, (b) electrochemical impedance at room temperature, and (c) Arrhenius plots.

density of the pellet is drastically increased for the CSP-LATP with 1 M acetic acid as an additive. In addition, neck growth is clearly seen in the CSP-LATP with acid, as presented in Figure 1e. In contrast to HTS-LATP, the particle sizes of CSP-LATP are still in the range of 300−400 nm.

The density of the as-obtained LATP pellets were measured by the Archimedes method, as listed in Figure S1 and Table S1. Relative densities are calculated in order to correlate them to the ionic conductivity of the pellets, as demonstrated in Figure 2a. Through electrochemical impedance spectroscopy, the ionic conductivities are investigated, as illustrated in Figure 2b. It is obvious that the ionic conductivity is linearly related to relative density, with higher densities resulting in increased ionic conductivity. The highest relative density of LATP 96 ± 2% is obtained for the pellet sintered at a high temperature of 1000 °C, and the lowest one is the LATP sintered by the dry-press method (74 ± 2%). For the two CSP-LATP pellets, the acid-assisted CSP-LATP reaches a high relative density of 93 ± 2%, while the water-assisted CSP-LATP is 79 ± 2% (Table S1). The CSP-LATP pellet with addition of acetic acid shows good sintering effects, with a density similar to the high-temperature sintering (relative density of 96 ± 2%).

As listed in Figure 2a and Table S1, the total ionic conductivity of HTS-LATP is 1.51×10^{-4} S cm^{-1} at room temperature, which is obtained by the intercepts of EIS spectra in Figure 2b at the X axis. LATP pellets prepared with the CSP process result in an ionic conductivity of 8.04×10^{-5} S cm^{-1} and 2.79×10^{-5} S cm^{-1} for the acid and water- assisted

processes, respectively. More importantly, the CSP-LATP with acid solution shows about five times higher ionic conductivity compared to the dry-press LATP electrolyte, which shows an ionic conductivity of 1.66×10^{-5} S cm^{-1}. The improvement of the ionic conductivity mainly comes from the grain boundary contribution, as presented in Figure 2b. The ionic conductivity dependencies of pellets against temperature are plotted as the Arrhenius plot in Figure 2c, with all samples showing good ionic conduction behavior. In addition, the temperature dependent EIS spectra of CSP-LATP is listed in Figure S2, the conductivities at different temperature are calculated based on the fitting data (Table S2). The activation energy of the pellet is calculated based on the slope of the plot, as listed in Table S1. CSP-LATP with acid shows an activation energy of 0.37 ± 0.02 eV, which is similar to the HTS-LATP at higher temperatures, while the dry-press LATP shows an activation energy of 0.45 ± 0.02 eV due to bad conduction at the grain boundary.

To better understand the structure of LATP solid electrolyte after sintering and the relationship between its properties and structure, the microstructure information is obtained through TEM images, as shown in Figure 3. For the CSP-LATP (acid), the particles are well sintered together, and only a small fraction of pores are observed (Figure 3a−c). The images indicate excellent densification of the LATP particles with CSP and post-annealing at medium temperature (650 °C). Looking closer, it is seen that the grain−grain interfaces still present some amorphous phases (Figure 3d, as marked by the dashed
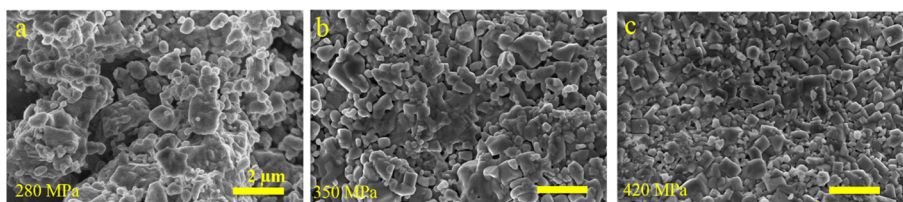
Figure 5. Pressure effect on cold sintered LATP. SEM images of the cold sintered pellet with different pressures: (a) 280 MPa, (b) 350 MPa, and (c) 420 MPa.
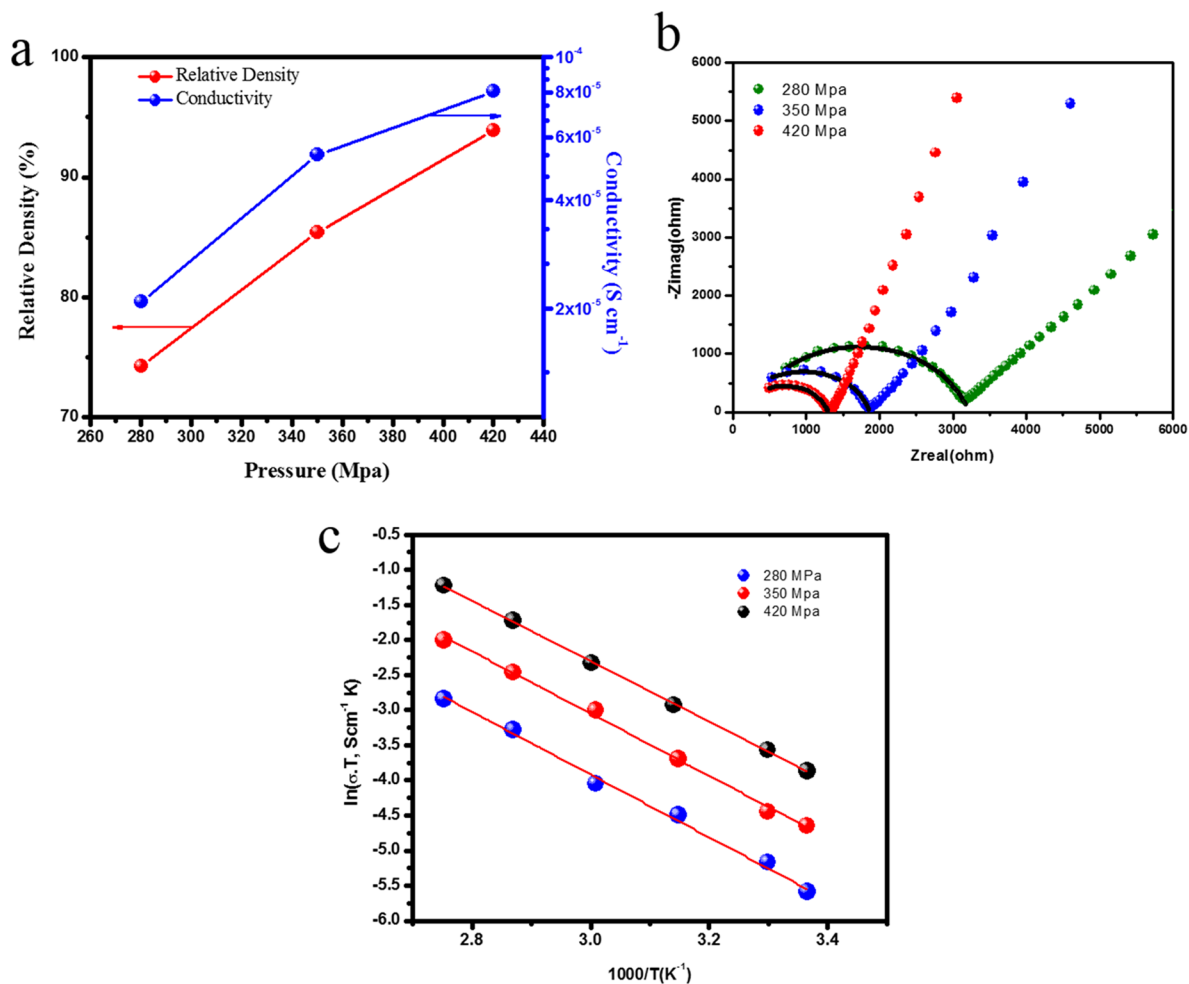

Figure 6. Pressure effect on cold sintered LATP. (a) Density and ionic conductivity of cold sintering LATP pellets with different pressure, (b) electrochemical impedance at room temperature, and (c) Arrhenius plots of LATP pellets against temperature pressed with different pressures.

line; and Figure S3). Additionally, nanometer-sized precipitates (crystals) in polygonal or round shapes are detected at the grain boundary regions (Figure 3e,f, as marked by the dashed line). EDS chemical mapping analysis reveals Al and Ti elements homogeneously distributed across the grains with no significant deviations in distribution, indicating the uniformity of chemical compositions at bulk and grain boundaries (Figure S4). Also, there shows no evidence of solvent residue. In the case of conventionally sintered LATP, the interconnected micron-sized grains are grown (Figure 3g) and a clean grain boundary is observed (Figure 3h,i). To evaluate the chemical information of the CSP-LATP pellet, XPS was conducted on the surface after firing at 650 °C. In Figure S5, the Ti is in still in 4+ state as expected. In addition, ICP was performed for the CSP-LATP pellet and LATP powders to understand the stoichiometry change during CSP and annealing processes. As

presented in Table S3, it shows that the elemental ratio does not change obviously after the CSP process.

To elucidate the influence of the liquid phase on the dissolution of the ions during the CSP process, different combinations of the solvent are investigated. As seen from Figure 4a, the LATP pellet with 1 M acetic acid and NMP solvent shows the highest relative density, while the pellet sintered with NMP shows the lowest relative density of 74 ± 2%, which is similar to the dry-press pellet. As illustrated in Figure S6, the particles in the NMP-assisted CSP-LATP are loosely packed, without formation of a neck between grains. As indicated by a recent study by Studart and Bouville, ion dissolution and liquid-induced plasticity do not occur in organic solvents, so there is no sintering behavior for the NMP solution.[21] Unfortunately, for the CSP process with pure water, the final pellet is easily cracked into pieces due to the rapid
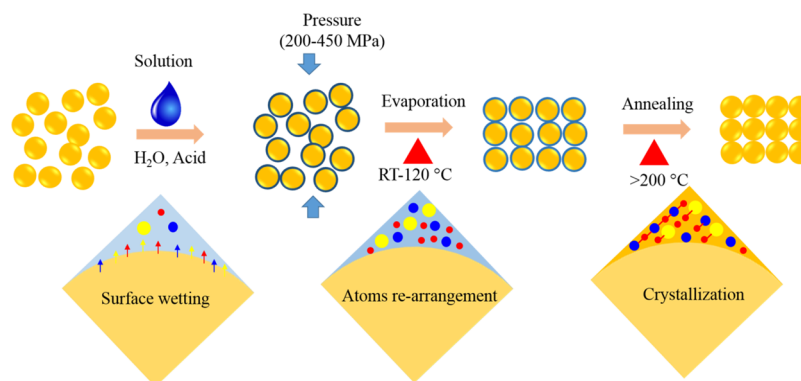
Figure 7. Schematic diagram of the cold sintering process.

evaporation of water at 120 °C (Figure S7a). To solve this problem, the inert NMP organic solvent is used as an additive, and a pellet with improved mechanical properties is obtained (Figure S7b). The reason is ascribed to the slowing of the evaporation rate of water (boil point of 100 °C) by incorporating the high boiling point NMP solvent (boil point of 202 °C). In order to verify the effect of the high boiling point organic solvent as an additive, DMSO with a boiling point of 189 °C is also used for comparison. The formed LATP pellet via CSP with 1 M acetic acid-DMSO can achieve a relative density of 84% and good mechanical integrity (Figure S1b and Figure S7a).

To determine the ionic conductivity, the EIS spectra of the LATP with different solutions are recorded and presented in Figure 4b. The conductivity of the NMP-assisted CSP-LATP shows an ionic conductivity of 2.07×10^{-5} S cm^{-1}, which is similar to the dry-press process (Table S4). For the LATP sintered with DMSO additive, the conductivity is about half of the LATP with NMP as the organic solvent coupled with acid solution. One possible reason is the lower boiling point of DMSO compared to NMP, which leads to a lower relative density of the CSP pellet due to the relatively higher water evaporation rate (Table S4). From the Arrhenius plots pictured in Figure 4c, the activation energy of the LATP pellet synthesized with DMSO and acetic acid is 0.39 ± 0.02 eV, which is lower than the pellet sintered with water and NMP (0.40 ± 0.02 eV) and pure NMP solution (0.41 ± 0.02 eV). The primary reason is that the acetic acid is effective in dissolving the edges of particles, which is also observed in the CSP process of ZnO.[22]

In a previous research, smaller particles were claimed to accelerate the densification process of ceramic materials.[11] Therefore, the LATP particles are ball-milled with ZrO$_2$ for 10 h before the CSP process. However, the ionic conductivity of the pellet only shows an ionic conductivity of 2.2×10^{-5} S cm^{-1}, even with a relative density is 81% (Figure S8). One possible reason for this observation may be the plastic deformation of the surface during the ball-milling process, which results in the formation of an amorphous phase on the surface, leading to a lower ionic conductivity.

Another important parameter in the CSP process is the applied stress. The evolution of the microstructure of the powders at different applied pressures was examined with SEM, as shown in Figure 5. At a low applied stress of 280 MPa, the agglomerates of nano-LATP particles are still visible and there is a large fraction of porosity due to the interagglomerate interstices. A higher applied stress of 350 MPa leads to a

significant densification and deformation of the agglomerates. This effect is more obvious when the applied stress is increased to 420 MPa, where agglomerates are invisible and only smaller porosity remains. The neck is formed between agglomerates with an increase of the relative density from 74% at 280 MPa to 93% at 420 MPa (Figure 5). More importantly, it should be noted that the densification of the agglomerates is not accompanied by the coarsening of particles, which is typically observed during sintering of ceramics at high temperatures (Figure 1b).

In line with an increase of the relative density, the conductivity of the LATP pellet is also increased, as illustrated in Figure 6a. EIS spectra in the Figure 6b indicates that the improvement in ionic conductivity is mainly attributed to the grain boundary, whereas the resistance of the grain is consistent at different applied stresses. The total conductivity of LATP electrolyte sintered at an applied stress of 280 and 350 MPa are 2.09×10^{-5} S cm^{-1} and 5.37×10^{-5} S cm^{-1}, respectively (Table S5). As shown in Figure 6c and Table S5, the activation energies of the LATP electrolyte sintered at an applied stress of 280 and 350 MPa are 0.39 ± 0.02 eV and 0.38 ± 0.02 eV, which are a little bit higher than the electrolyte sintered at an applied pressure of 420 MPa. These results suggest that pellets with high ionic conductivity are achieved with high applied stress, leading to higher relative densities and lower activation energy.

Overall, the cold sintering process of LATP involves different mass-transport pathways, as schematically depicted in Figure 7. First, the surface atoms LATP particles are dissolved congruently into water or acidic solution. Then, ions migrate due to the driving force of high-stress concentrations at contact points by applying an external stress. The dissolved ions at the contact point diffuse at the contact region, undergo rearrangement, and finally precipitate by evaporation of the water molecules. Therefore, an amorphous phase is quenched at the grain boundary at the end of evaporation. To increase the crystallinity and density of the as-obtained pellet, post-annealing at medium temperature is used to reduce the amorphous phase at the grain boundaries.

■ CONCLUSIONS

In this work, Lithium-ion conductor $Li_{1.3}Al_{0.3}Ti_{1.7}(PO_4)_3$ (LATP) is densified with a novel cold sintering process (CSP). CSP is a compacting process requiring a low temperature and short sintering time, which can be widely applied to other inorganic materials. In this work, the obtained LATP electrolyte is synthesized via an optimized CSP process

and can achieve an ionic conductivity of 8.04×10^{-5} S cm^{-1} with an activation energy of 0.37 eV. HRTEM analysis shows that some nanoprecipitate forms at the grain boundaries in the CSP-LATP, while the HTS-LATP shows a clean grain boundary. With nanocrystalline in the grain boundary, some lithium-ion conduction channels are formed, which can improve the ionic conductivity of cold sintered samples. The current study shows that the density of a solid electrolyte is highly related to the sintering process, solvent addition, and applied stress. Although there are still challenges in understanding the change in the surface chemistry of particles undergoing the CSP process, this new technique gives a new direction in preparing solid-state electrolytes and solid-state batteries with low costs and high efficiencies.

■ ASSOCIATED CONTENT

Ⓢ Supporting Information

The Supporting Information is available free of charge on the ACS Publications website at DOI: 10.1021/acsami.9b08132.

> Experimental details, additional physical, and electrochemical characterization (PDF)

■ AUTHOR INFORMATION

Corresponding Authors
*E-mail: xpsong@skl.ustb.edu.cn (X. Song).
*E-mail: xsun9@uwo.ca (X. Sun).

ORCID Ⓞ
Xueliang Sun: 0000-0003-2881-8237

Notes
The authors declare no competing financial interest.

■ ACKNOWLEDGMENTS

■ REFERENCES

(1) Xu, K. Electrolytes and Interphases in Li-Ion Batteries and Beyond. *Chem. Rev.* **2014**, *114*, 11503−11618.

(2) Umeshbabu, E.; Zheng, B.; Yang, Y. Recent Progress in All-Solid-State Lithium− Sulfur Batteries Using High Li-Ion Conductive Solid Electrolytes. *Electrochem. Energy Rev.* **2019**, *3*, 1−32.

(3) Quartarone, E.; Mustarelli, P. Electrolytes for Solid-State Lithium Rechargeable Batteries: Recent Advances and Perspectives. *Chem. Soc. Rev.* **2011**, *40*, 2525−2540.

(4) Bachman, J. C.; Muy, S.; Grimaud, A.; Chang, H.-H.; Pour, N.; Lux, S. F.; Paschos, O.; Maglia, F.; Lupart, S.; Lamp, P.; Giordano, L.; Shao-Horn, Y. Inorganic Solid-State Electrolytes for Lithium Batteries: Mechanisms and Properties Governing Ion Conduction. *Chem. Rev.* **2016**, *116*, 140−162.

(5) Tan, S.-J.; Zeng, X.-X.; Ma, Q.; Wu, X.-W.; Guo, Y.-G. Recent Advancements in Polymer-Based Composite Electrolytes for Rechargeable Lithium Batteries. *Electrochem. Energy Rev.* **2018**, *1*, 113−138.

(6) Knauth, P. Inorganic Solid Li Ion Conductors: An Overview. *Solid State Ionics* **2009**, *180*, 911−916.

(7) Zhang, Z.-H.; Liu, Z.-F.; Lu, J.-F.; Shen, X.-B.; Wang, F.-C.; Wang, Y.-D. The Sintering Mechanism in Spark Plasma Sintering − Proof of the Occurrence of Spark Discharge. *Scr. Mater.* **2014**, *81*, 56−59.

(8) Aboulaich, A.; Bouchet, R.; Delaizir, G.; Seznec, V.; Tortet, L.; Morcrette, M.; Rozier, P.; Tarascon, J.-M.; Viallet, V.; Dollé, M. A New Approach to Develop Safe All-Inorganic Monolithic Li-Ion Batteries. *Adv. Eng. Mater.* **2011**, *1*, 179−183.

(9) Guo, J.; Guo, H.; Baker, A. L.; Lanagan, M. T.; Kupp, E. R.; Messing, G. L.; Randall, C. A. Cold Sintering: A Paradigm Shift for Processing and Integration of Ceramics. *Angew. Chem., Int. Ed.* **2016**, *55*, 11457−61.

(10) Guo, J.; Berbano, S. S.; Guo, H.; Baker, A. L.; Lanagan, M. T.; Randall, C. A. Cold Sintering Process of Composites: Bridging the Processing Temperature Gap of Ceramic and Polymer Materials. *Adv. Funct. Mater.* **2016**, *26*, 7115−7121.

(11) Guo, H.; Baker, A.; Guo, J.; Randall, C. A. Protocol for Ultralow-Temperature Ceramic Sintering: An Integration of Nano-technology and the Cold Sintering Process. *ACS Nano* **2016**, *10*, 10606−10614.

(12) Guo, H.; Guo, J.; Baker, A.; Randall, C. A. Hydrothermal-Assisted Cold Sintering Process: A New Guidance for Low-Temperature Ceramic Sintering. *ACS Appl. Mater. Interfaces* **2016**, *8*, 20909−15.

(13) Nakaya, H.; Iwasaki, M.; de Beauvoir, T. H.; Randall, C. A. Applying Cold Sintering Process to a Proton Electrolyte Material: CsH$_2$PO$_4$. *J. Eur. Ceram. Soc.* **2019**, *39*, 396−401.

(14) Liu, Y.; Sun, Q.; Wang, D.; Adair, K.; Liang, J.; Sun, X. Development of the Cold Sintering Process and Its Application in Solid-State Lithium Batteries. *J. Power Sources* **2018**, *393*, 193−203.

(15) Wang, D.; Sun, Q.; Luo, J.; Liang, J.; Sun, Y.; Li, R.; Adair, K.; Zhang, L.; Yang, R.; Lu, S.; Huang, H. Mitigating the Interfacial Degradation in Cathodes for High-Performance Oxide-Based Solid-State Lithium Batteries. *ACS Appl. Mater. Interfaces* **2019**, *11*, 4954−4961.

(16) Leng, H.; Huang, J.; Nie, J.; Luo, J. Cold Sintering and Ionic Conductivities of Na$_{3.256}$Mg$_{0.128}$Zr$_{1.872}$Si$_2$PO$_{12}$ Solid Electrolytes. *J. Power Sources* **2018**, *391*, 170−179.

(17) Guo, J.; Zhao, X.; Herisson De Beauvoir, T.; Seo, J. H.; Berbano, S. S.; Baker, A. L.; Azina, C.; Randall, C. A. Recent Progress in Applications of the Cold Sintering Process for Ceramic−Polymer Composites. *Adv. Funct. Mater.* **2018**, *28*, 1801724.

(18) Guo, J.; Baker, A. L.; Guo, H.; Lanagan, M.; Randall, C. A. Cold Sintering Process: A New Era for Ceramic Packaging and Microwave Device Development. *J. Am. Chem. Soc.* **2017**, *100*, 669−677.

(19) Berbano, S. S.; Guo, J.; Guo, H.; Lanagan, M. T.; Randall, C. A. Cold Sintering Process of Li1.5Al0.5Ge1.5(PO4)3solid Electrolyte. *J. Am. Chem. Soc.* **2017**, *100*, 2123−2135.

(20) Aono, H.; Sugimoto, E.; Sadaoka, Y.; Imanaka, N.; Adachi, G.-Y. Dc Conductivity of Li$_{1.3}$Al$_{0.3}$Ti$_{1.7}$(PO$_4$)$_3$ Ceramic with Li Electrodes. *Chem. Lett.* **1991**, 1567−1570.

(21) Bouville, F.; Studart, A. R. Geologically-Inspired Strong Bulk Ceramics Made with Water at Room Temperature. *Nat. Commun.* **2017**, *8*, 14655.

(22) Funahashi, S.; Guo, J.; Guo, H.; Wang, K.; Baker, A. L.; Shiratsuyu, K.; Randall, C. A. Demonstration of the Cold Sintering Process Study for the Densification and Grain Growth of ZnO Ceramics. *J. Am. Chem. Soc.* **2017**, *100*, 546−553.